Passivation Properties and Formation Mechanism of Amorphous Halide Perovskite Thin Films

Rigter, Susan A.; Quinn, Xueying L.; Kumar, Rishi E.; Fenning, David P.; Massonnet, Philippe; Ellis, Shane R.; Heeren, Ron M. A.; Svane, Katrine Louise; Walsh, Aron; Garnett, Erik C.

Published in:
Advanced Functional Materials

Link to article, DOI:
10.1002/adfm.202010330

Publication date:
2021

Document Version
Version created as part of publication process; publisher's layout; not normally made publicly available

ADVANCED FUNCTIONAL MATERIALS
www.afm-journal.de

Passivation Properties and Formation Mechanism of Amorphous Halide Perovskite Thin Films

*Susan A. Rigter, Xueying L. Quinn, Rishi E. Kumar, David P. Fenning, Philippe Massonnet, Shane R. Ellis, Ron M. A. Heeren, Katrine L. Svane, Aron Walsh, and Erik C. Garnett**

Lead halide perovskites are among the most exciting classes of optoelectronic materials due to their unique ability to form high-quality crystals with tunable bandgaps in the visible and near-infrared using simple solution precipitation reactions. This facile crystallization is driven by their ionic nature; just as with other salts, it is challenging to form amorphous halide perovskites, particularly in thin-film form where they can most easily be studied. Here, rapid desolvation promoted by the addition of acetate precursors is shown as a general method for making amorphous lead halide perovskite films with a wide variety of compositions, including those using common organic cations (methylammonium and formamidinium) and anions (bromide and iodide). By controlling the amount of acetate, it is possible to tune from fully crystalline to fully amorphous films, with an interesting intermediate state consisting of crystalline islands embedded in an amorphous matrix. The amorphous lead halide perovskite has a large and tunable optical bandgap. It improves the photoluminescence quantum yield and lifetime of incorporated crystalline perovskite, opening up the intriguing possibility of using amorphous perovskite as a passivating contact, as is currently done in record efficiency silicon solar cells.

1. Introduction

Lead halide perovskites form an emerging class of semiconductors that have garnered great attention in the past several years due to their rapid rise from obscurity to current use in solar cells with power conversion efficiencies above 20%.[1] The success of thin film perovskite solar cells can be ascribed to a combination of factors including a relatively high carrier mobility, long diffusion length, low effective mass, high photoluminescence quantum yield (PLQY), and strong absorption onset.[2] High quality halide perovskite thin films can be fabricated easily, using a low temperature solution process, because the material's low formation energy allows for easy crystallization.[3]

Surprisingly, despite the rapid and facile crystallization of these ionic semiconductors, researchers have occasionally encountered an amorphous phase of lead halide perovskite. The formation of amorphous methylammonium (MA) lead halide nanoparticles was reported, formed by hot injection of a precursor solution with ligands into toluene.[4] PbX_6 octahedra were observed to be present in the precursor solution, which are generally understood to determine the energy levels of the optical bandgap,[5] and accordingly, the bandgaps of the resulting nanocrystals were tunable by varying the composition of halides, although oddly the bandgap seemed to correspond to the crystalline counterpart. The formation mechanism

S. A. Rigter, Prof. E. C. Garnett
Center for Nanophotonics
AMOLF
Science Park 104, Amsterdam 1098 XG, The Netherlands
E-mail: E.Garnett@amolf.nl
S. A. Rigter, Prof. E. C. Garnett
Institute of Physics
University of Amsterdam
Science Park 904, Amsterdam 1098 XH, The Netherlands
X. L. Quinn, Prof. D. P. Fenning
Sustainable Power and Energy Center
University of California, La Jolla
San Diego, CA 92093, USA
X. L. Quinn, R. E. Kumar, Prof. D. P. Fenning
Materials Science and Engineering Program
University of California, La Jolla
San Diego, CA 92093, USA
R. E. Kumar, Prof. D. P. Fenning
Department of Nanoengineering
University of California, La Jolla
San Diego, CA 92093, USA
Dr. P. Massonnet, Dr. S. R. Ellis, Prof. R. M. A. Heeren
Maastricht MultiModal MolecularImaging Institute (M4I)
Maastricht University
Maastricht 6229 ER, The Netherlands
Dr. K. L. Svane
Department of Energy Conversion and Storage
Technical University of Denmark
Kgs. Lyngby 2800, Denmark
Prof. A. Walsh
Department of Materials Science and Engineering
Yonsei University
Seoul 03722, Korea
Prof. A. Walsh
Department of Materials
Imperial College London
London SW7 2AZ, UK

The ORCID identification number(s) for the author(s) of this article can be found under https://doi.org/10.1002/adfm.202010330.

DOI: 10.1002/adfm.202010330

was unclear, with only the remark that the presence of octylamine in the precursor solution could help form amorphous particles. $CsPbBr_3$ quantum dots with a crystalline core and amorphous shell were synthesized.[6] The amorphous shell protected the crystalline core against detrimental environmental influences, such as humidity, oxygen and radiative corrosion, as well as contributing to exciton formation, although the optical properties of the crystalline and amorphous phase could not be studied independently due to their close spatial proximity. An amorphous phase has also been suggested in mixed-halide $MAPbBr_{1.5}I_{1.5}$ perovskite films.[7] Using ^{207}Pb NMR, a signal of a pure $MAPbBr_3$ phase was measured in solution processed samples, that could not be accounted for by X-ray diffraction (XRD) or steady-state optical measurements. This amorphous perovskite phase made up 26–74% of the sample. Additionally, amorphization of $MAPbBr_3$ perovskite crystals was observed as an effect of hydrostatic pressure.[8] Under increasing hydrostatic pressure, the perovskite transformed from a cubic *pm3m* space group into cubic *Im3* at 0.4 GPa, then into orthorhombic *Pnma* at 1.89 GPa, and finally, amorphization occurred around 4 GPa. All phase changes were reversible. The amorphization appeared to be caused by a tilting of the octahedra. Due to the deformation of bonds between Pb and Br, the bandgap increases slightly upon amorphization (+0.2 meV). Finally, amorphous perovskite at grain boundaries of $MAPbBr_3$ perovskite thin films was observed in our lab.[9] The amorphous material was characterized by electron backscatter diffraction and nano-X-ray diffraction (nano-XRD), and for both techniques no signal of crystallinity was measured. The photoluminescence (PL) signal measured at these amorphous regions showed a lifetime up to thrice longer than that of the grain interiors, as well as enhanced PL intensity. The PL quantum yield of those regions has since been measured and indeed is higher than the crystalline grain interiors (Section S1, Supporting Information). The beneficial properties observed in several of the studies along with the well-known example of amorphous Si passivation in record crystalline silicon solar cells, suggest amorphous perovskites could be useful in optoelectronic devices.[10] However, the inability to tune from fully crystalline to fully amorphous halide perovskite films at ambient pressure made it difficult to verify the presence or distribution of the amorphous phase, study its properties, formation mechanism, and influence on crystalline halide perovskite.

The previous inability to form amorphous perovskite thin films is not surprising given their ionic nature. Ions in a solution have a high propensity to crystallize, causing the crystallization to occur much faster than for covalent solids.[11] For example, to obtain an amorphous salt from a brine, the solvent and the ions need to be separated quickly, via one of two methods. First, one can directly precipitate the ions from the brine. This is possible under non-equilibrium conditions, caused by, for example, an antisolvent, or environmental factors such as low relative humidity, a quick drop in temperature, or low pressure. Second, one can quickly remove the solvent from the ions. In this case, the ions, which originally were coordinated with the solvent "collapse" into an amorphous state.[12] These two routes of rapid desolvation are realizations of the following requirement:

$$R_{\text{growth}} > R_{\text{crystallization}} \quad (1)$$

where R_{growth} is the rate of growth of the solid and $R_{\text{crystallization}}$ the rate of crystallization. If the components of the solid precipitate faster than they can form a crystal, the material will be amorphous. To satisfy this condition, the rate of crystallization can be decreased, for example, by inhibiting the crystallization reaction, or the rate of growth can be increased, by increasing the speed of desolvation.

Here, we show that rapid desolvation of a crystalline intermediate provides a method to form crystalline, amorphous, and mixed-phase halide perovskite films of a variety of compositions. The amorphous perovskite films have large and tunable bandgaps, and improve the properties of crystalline inclusions. The formation of amorphous perovskite is aided by addition of methylammonium acetate (MAAc) to the synthesis. The presence of MAAc has previously been shown to improve crystalline film quality, improve photovoltaic performance, take part in an intermediate phase, and causes the incorporation of acetate into several perovskite compositions.[13] Herein it is shown that the addition of more MAAc during synthesis both inhibits the crystallization reaction, and increases the rate of desolvation, leading to formation of amorphous perovskite films and the incorporation of acetate in the films. The promising passivating properties of these films on crystalline perovskite, along with recent results using amorphous tin halide films to improve perovskite solar cells,[14] bring up the intriguing possibility of using amorphous passivating contacts for record solar cell performance, as has been demonstrated with crystalline silicon.[10,15]

2. Results and Discussion

Figure 1a shows powder-XRD spectra of samples prepared via a previously reported method for creating $MAPbBr_3$ thin films,[13a] for which a percentage of methylammonium bromide (MABr) is replaced with MAAc (sample name $= \frac{[\text{MAAc}]}{[\text{MABr}]+[\text{MAAc}]} \times 100\%$). What stands out immediately is the presence of a broad amorphous hump for samples 46.7%, 60%, and 66.7%. These samples do not show the characteristic peaks for ⟨001⟩ $MAPbBr_3$, which are visible for samples 33.3%, 40%, and 53.3%, as well as for the reference sample 0%. The same hump is visible for sample 40%, albeit below crystalline peaks. Such a broad hump is characteristic for amorphous materials, or materials with order on a lower scale than the measurement precision.[16] Applying the Scherrer equation to the amorphous humps, demonstrates that there is a coherence length on the order of a nanometer within the samples (Section S2, Supporting Information). This is close to the size of a lead halide cage, which could be present in the material. The orientation of crystalline perovskite of the reference sample is ⟨001⟩, and does not change upon addition of MAAc. However, when annealing amorphous perovskite above their crystallization temperature, it crystallizes preferentially in a ⟨210⟩ orientation (Section S3, Supporting Information).

The variation in crystallinity between samples 53.3% and 46.7% is eye-catching. This result was reproducible using the same precursor solution, in spite of close control of the amounts of precursors and concentration of the solution. There appears to be a transition range between amorphous and partially crystalline films. Close to this transition range, the crystallinity of

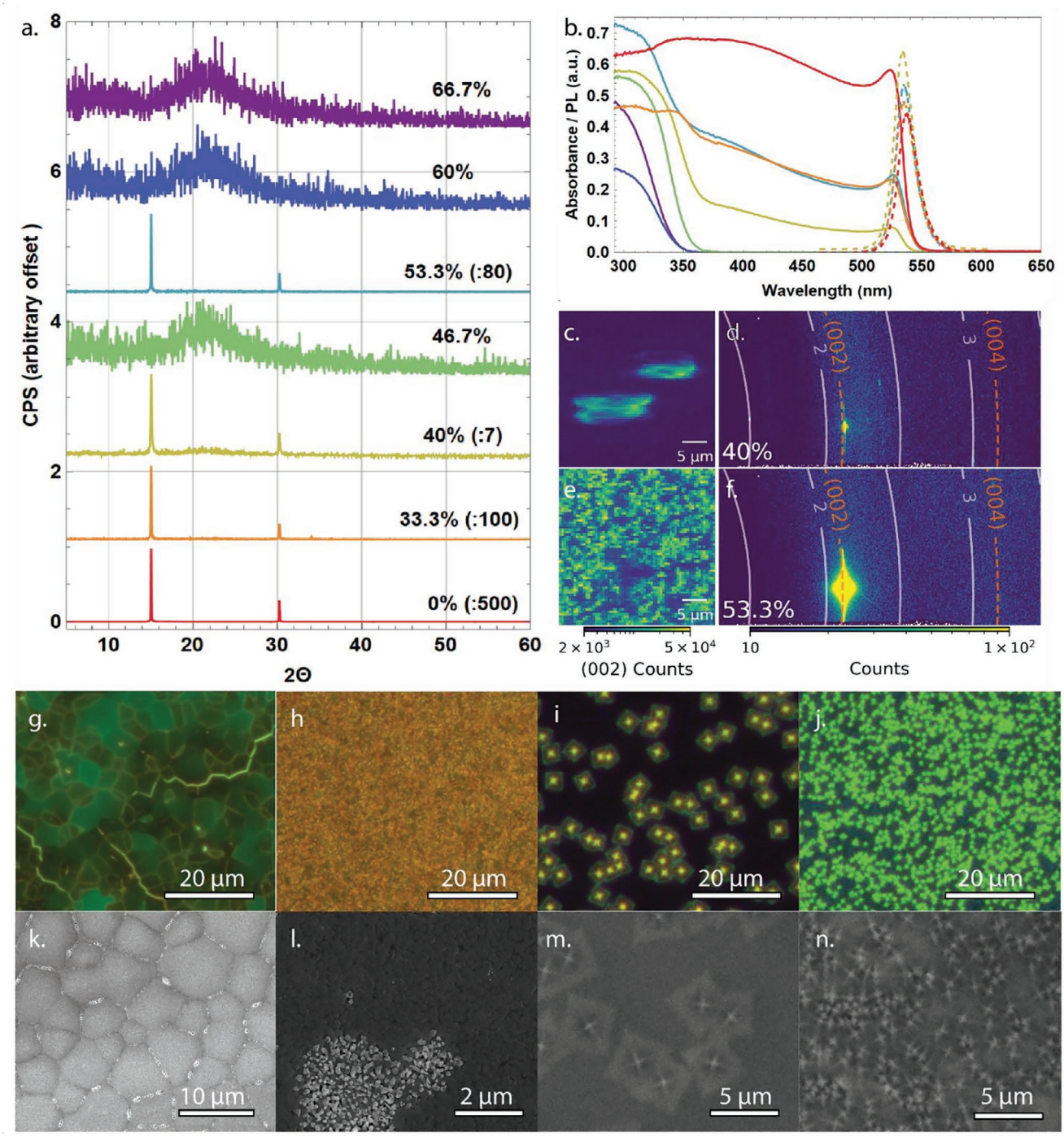

Figure 1. a) XRD patterns, b) absorption, and PL spectra of all samples. c,e) Nano-XRD spatial (002) scattering intensity of sample 40% and 53.3%, and d,f) corresponding diffraction patterns, integrated over an area of 2500 μm^2. White arcs indicate scattering magnitudes in inverse angstroms, while the orange dashed arcs highlight the diffraction expected from crystalline domains. g–j) Dark-field optical images and k–n) SEM images of samples 0%, 33.3%, 40%, and 53.3%, respectively.

the final sample depends strongly on impurity levels in the precursor solution (Section S4, Supporting Information). As is previously reported for mixed-cation and mixed-halide perovskites, the composition of halide perovskite films does not have a one-to-one relationship to the composition of the precursor solution.[17] The absorbance and emission spectra show that each sample that contains crystalline areas exhibits a direct optical bandgap in the visible at 538 nm (2.3 eV), the reported optical bandgap for $MAPbBr_3$ thin films (Figure 1b).[13a] Each of these samples also exhibits PL in the same wavelength range, with negligible shifts between the peak positions of the samples. More interestingly, the XRD-amorphous samples have an

absorption onset in the UV, each with a bandgap bigger than 3.3 eV, and slightly increasing with higher MAAc percentages (Section S5, Supporting Information).

A blueshift of the optical bandgap was previously reported to be caused by the breaking of bonds between lead and bromide.[8] However, the observed bandgap increase as an effect of that is much smaller than observed here, and we therefore conclude that this alone cannot cause the large shift. There are two more likely explanations for the observation. First, a blueshift of the optical bandgap is predicted by density functional theory (DFT) for crystalline $MAPbBr_3$ perovskite, already when one in 24 bromide ions in the lattice is replaced by an acetate ion. When bromide is fully replaced by acetate in the perovskite lattice, the predicted bandgap increases by 2.8 eV (Section S6, Supporting Information). The bandgap of perovskite depends on the energy levels of the lead–halide octahedra.[18] When acetate partially substitutes bromide in the perovskite lattice, the bandgap of the material depends on the lead–bromide–acetate octahedra. Second, the blue shift could be caused by quantum confinement. If lead–bromide octahedra are present in the material but without the extended ordering in crystalline materials, this could be modeled as a nanocrystalline material with a grain size equal to that of the octahedra. In such a case, there will be strong quantum confinement, with an expected bandgap increase of up to 3 eV (Section S7, Supporting Information). Both of these scenarios rely on the assumption that lead–bromide octahedra are present in the material.

Figures 1g–j and 1k–m show optical microscopy images and scanning electron microscopy (SEM) images of samples with at least some crystalline XRD signal, respectively. The amorphous samples are not shown in this figure, since they were very smooth and provided no contrast in either optical or SEM images (Section S8, Supporting Information). The reference sample 0% is a thin film with relatively large domain size, appearing smooth in both optical microscopy and SEM (Figure 1g,k). When 33.3% MAAc is added, a small domain size film forms, with some areas that show contrast in SEM (Figure 1h,l). The origin of this contrast is unknown, but could be caused by surface roughness or contrast between underlying grains. Figure 1i,m shows sample 40%, which indeed shows what appears to be a combination of crystalline inclusions and an amorphous matrix. Sample 53.3% looks similar (Figure 1j,n), with a higher density of smaller crystalline inclusions. This observation correlates well with the absorbance spectra, as well as with absorbance and PL maps of sample 40% (Section S9, Supporting Information) and with secondary ion mass spectroscopy (SIMS) and nano-XRD maps which will be discussed later. There are three samples which both have an absorption onset in the visible and in the UV, most strongly visible for samples 40% and 53.3%. The onset in the visible originates from crystalline perovskite, while the onset in the UV corresponds to the absorbance onset for the fully amorphous films.

To investigate spatial crystallographic properties of the samples, nano-XRD was used. Figures 1c and 1e are spatial maps of the diffraction intensity of the 002 peak of samples 40% and 53.3%, respectively. It is visible that there is a large variation in diffraction intensity within these samples. This confirms the hypothesis that these samples contain coexisting amorphous and crystalline material. Scattering patterns from individual points within amorphous and crystalline areas are shown in Section S10, Supporting Information. Figures 1d and 1f show the integrated scattering from microdiffraction measurements over 2500 μm^2 areas of sample 40% and 53.3%, respectively. Qualitatively, it is similar to the XRD spectrum of the same sample, with a sharp peak resulting from ⟨002⟩ crystalline perovskite planes, and a broad background, resulting from amorphous material.

Various methods were used to examine the composition of the samples. The results of energy dispersive X-ray spectroscopy (EDS) measurements can be found in **Figure 2**a. These spectra are integrated from maps collected over an area of at least 18 μm^2. There is no apparent difference between crystalline and amorphous areas within the same sample (Section S11, Supporting Information). Each of the atoms necessary to form $MAPbBr_3$ perovskite is present in each sample, independent of crystallinity. Furthermore, there is a large increase of the silicon peak resulting from the substrate with increasing MAAc addition. A larger silicon signal could be the result of thinner films or a larger electron penetration depth for the amorphous material. Additionally, there is a paired decrease of the bromide peak and increase of the oxygen and carbon peaks upon addition of more MAAc. This observation suggests that acetate gets incorporated into the films replacing bromide, both in crystalline and amorphous areas. This hypothesis is confirmed by X-ray photoelectron spectroscopy (Section S12, Supporting Information) and SIMS.

Figure 2b shows a map of the ratio of acetate to bromide for each sample, and a plot of the average ratio as a function of the percentage of acetate to bromide added during sample fabrication. These ratios were measured by SIMS. In spite of the large error bars, it is possible to conclude that the ratio of acetate to bromide goes up roughly linearly with the ratio of acetate and bromide precursors used during fabrication. However, for samples 0% and 33.3%, virtually no acetate was incorporated. It seems there is a threshold of acetate that is present during fabrication, below which no acetate gets incorporated into the final films. Above the threshold, the incorporation efficiency is increased and the amount of acetate increases linearly with increasing addition of acetate to the synthesis.

Only within the maps for samples 40% and 53.3%, a significant contrast is visible. There are some areas in the samples that show a higher measured ratio of Ac:Br than the rest of the sample. Surprisingly, especially for the 40% sample, these areas seem to correspond with the crystalline inclusions. This could have three origins: the crystalline areas contain a higher ratio of acetate to bromide, the acetate gets excluded from the crystalline area during nucleation such that the surface of crystallites have a locally higher acetate concentration, or the ratio between the sputter yield of acetate and that of bromide is higher for crystalline materials. The latter seems the most likely, as bromide ions are, presumptively, bound more strongly in a full crystalline lattice, than in single lead halide octahedra. This makes it more likely to sputter off a bromide ion in amorphous material than in crystalline material, making the ratio of measured acetate to bromide ions increase. However, further studies with higher resolution SIMS, frozen samples (to reduce

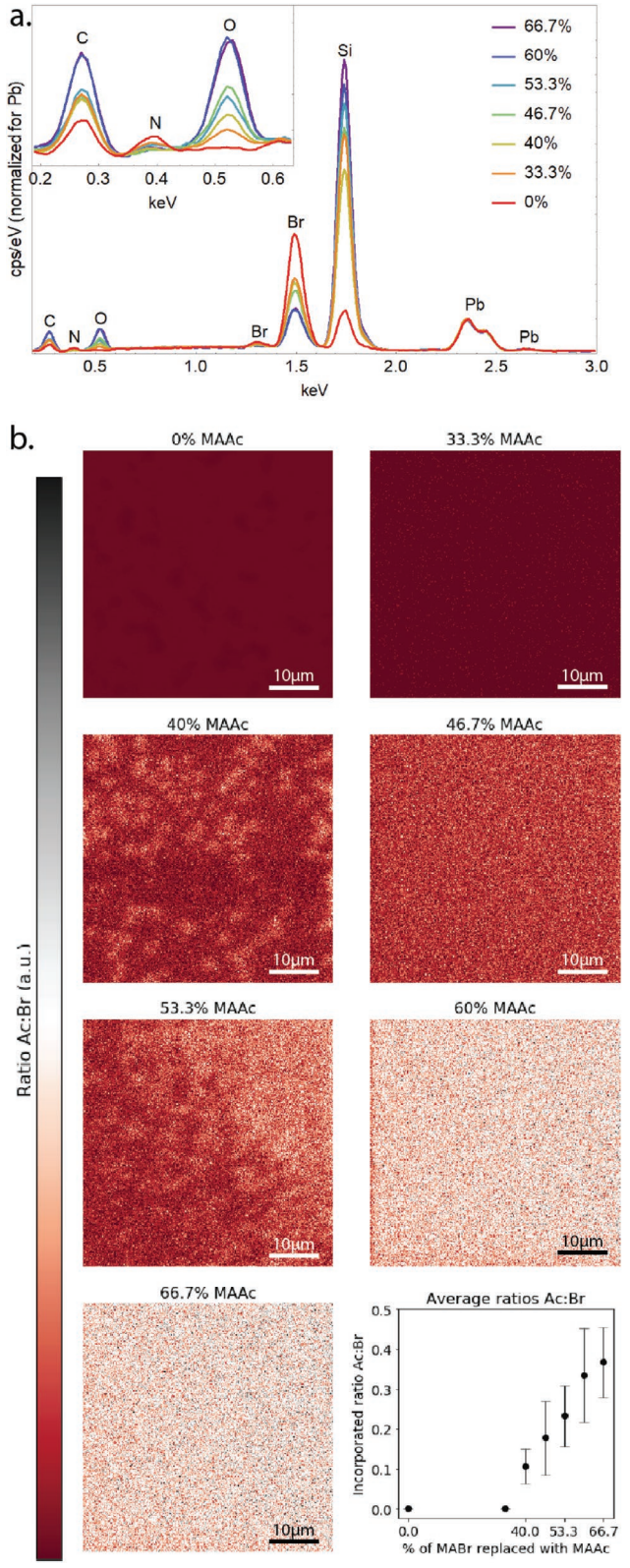

Figure 2. a) EDS spectra of samples with different amounts of MABr replaced with MAAc and a zoom-in of the low energy region (inset). The Si peak originates from the substrate. b) Negative mode SIMS maps of ratios Ac:Br for the samples, and a plot of the relationship between added and incorporated ratios Ac:Br.

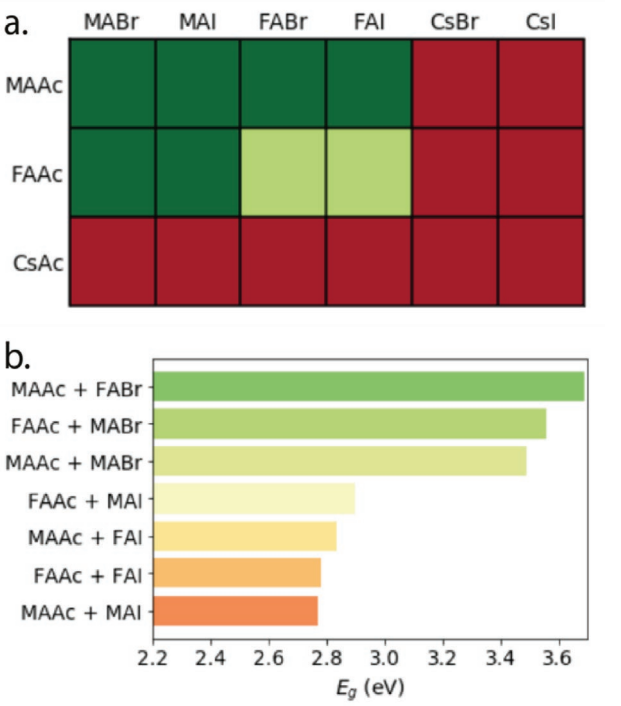

Figure 3. a) Map of precursor combinations and their product when processed using the method described, and b) the bandgaps of the resulting amorphous perovskite.

the local mixing during sputtering) and careful calibration of sputter yield are needed to be certain.

Formation of amorphous perovskite by adding an organic acetate precursor is not limited to $MAPbBr_3$ perovskites. **Figure 3**a provides an overview of what compositions of amorphous perovskite can be made via spin coating a solution of the precursors in dimethyl sulfoxide (DMSO). All the combinations of methylammonium, formamidinium, iodide, and bromide can lead to either fully or partially amorphous thin films, while the Cs cation inhibits amorphous film formation, mostly due to poor precursor solubility (Sections S13 and S14, Supporting Information). The two films with formamidinium acetate (FAAc) and formamidinium halide precursors show weak XRD peaks of crystalline perovskite, as well as an amorphous hump.[19] The peaks of crystalline perovskite can be attributed to formation of small amounts of $FAPbX_3$ or $FAPb(X_{3-x}Ac_x)$ perovskite within an amorphous film, indicating slight differences in the transition range when varying the organic acetate precursor to form amorphous perovskite. The material resulting from a combination of FAAc, FABr, and lead acetate ($PbAc_2$) has two absorption edges, similar to the material combining crystalline and amorphous $MAPbBr_3$. The regular inorganic–organic lead bromide perovskite bandgap of 2.3 eV is present, as well as an absorption edge in the UV (Section S5, Supporting Information).

Each of the amorphous perovskite films has a higher optical bandgap than is reported for their crystalline counterparts (Figure 3b).[20] Presumably, this shift occurs in the same way as for amorphous $MAPbBr_3$, in which either quantum confinement within lead bromide octahedra occurs, or replacement of

Br by Ac in these octahedra occurs. It is especially interesting to compare the bandgaps of each of these amorphous perovskites. For each organic cation, the iodide has a smaller bandgap than the bromide, analogous with crystalline perovskites.[21] This is because the bandgap is still determined primary by the lead halide/acetate octahedra in the amorphous material.

Section S15, Supporting Information, shows EDS spectra of the samples with varying precursors. Similarly to the composition of amorphous $MAPbBr_3$, all atoms necessary to form crystalline halide perovskite are present, as well as a substantial amount of oxygen and carbon. From this we conclude that in these films acetate was also incorporated into the amorphous material.

Interestingly, films containing both crystalline and amorphous perovskites (40% and 53%) display superior emission compared to a fully polycrystalline reference sample (0%). **Figure 4**a shows PLQY maps of these mixed samples and a polycrystalline reference. The reference sample has an average PLQY of 8% and peak value of 11%. The same average value is measured for the sample with a low density of crystalline incorporations (40%), but the peak value of 13% is significantly higher. Looking at the map and histogram, it appears that the average in the 40% sample is brought down by areas that are largely amorphous and therefore not contributing directly to absorption or emission. Collection losses in our system for emission happening far away from the excitation spot are likely responsible for these low PLQY pixels. This hypothesis is supported by the results for the 53.3% sample where crystalline and amorphous regions are mixed at a length scale smaller than our diffraction limited spatial resolution. In that case, the average PLQY is 16.6%, over twice the value for the reference sample, with a much narrower range of PLQY values.

The increase of PLQY when crystalline material is incorporated in an amorphous matrix, could be caused by three different mechanisms: more efficient outcoupling, a decrease of deep trap states, or surface passivation. First, more efficient light outcoupling would increase the amount of measured photons, but would not increase the carrier lifetime. Figure 4b shows that the films with mixed amorphous and crystalline perovskites (40% and 53.3%) show not only higher PLQY, but also longer lifetimes compared to the fully crystalline (0% and 33.3%) samples. This demonstrates that there was an increase in the ratio of radiative to non-radiative decay rates, and rules out more efficient light outcoupling as the sole reason for the increase in PLQY. Second, a decrease in deep trap states could be caused by the gettering of deep traps in the amorphous material. It is likely that the formation energy of an ion vacancy or an interstitial is lower in the amorphous material, and will therefore be gettered there. This would lead to a higher quality crystalline material when an amorphous matrix is present. Third, the surface of the crystalline phase might be passivated by the amorphous matrix. The interface between the crystalline and amorphous perovskite possibly hosts fewer dislocations, dangling bonds, and strain than the interfaces present in the polycrystalline sample (crystal–crystal, crystal–air, and crystal–substrate). Currently, it is not possible to discern between the latter two mechanisms, nor is it possible to rule out a coexistence of all three mechanisms.

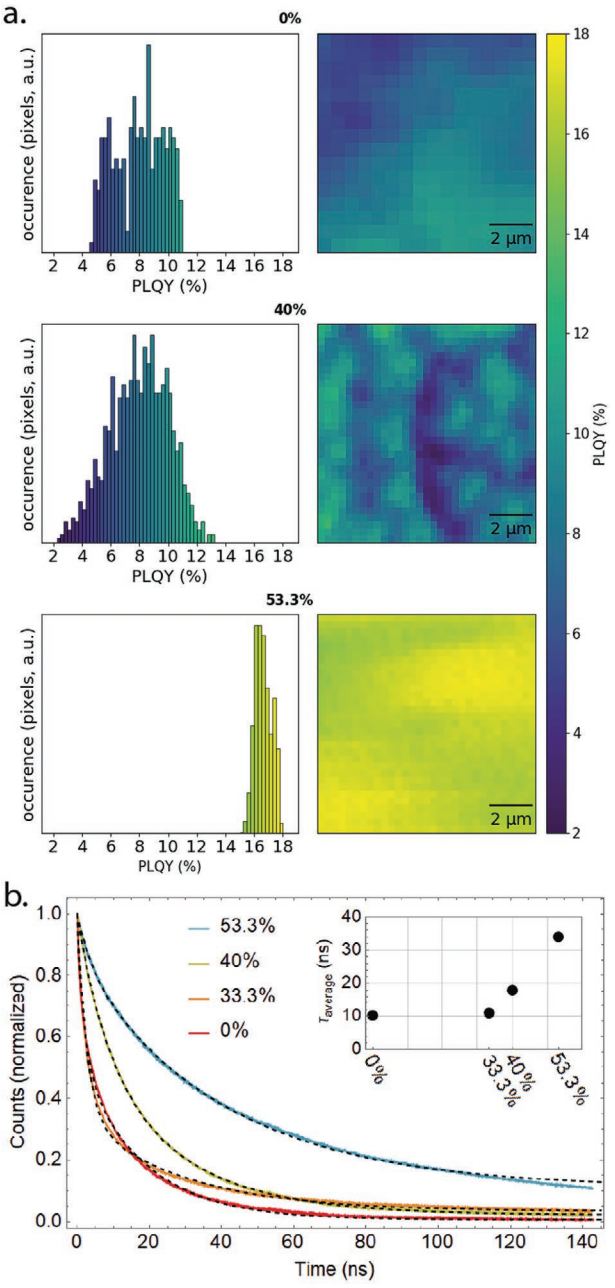

Figure 4. a) PLQY histograms and PLQY maps (λ_{exc} = 460 nm). b) Time-resolved PL decays of samples with certain percentages of MABr replaced with MAAc (λ_{exc} = 488 nm). Inset in (b): average PL lifetime of each sample.

Given the generality of amorphous perovskite films and their positive effects on optical properties and stability, it is interesting to consider the formation mechanism. The method used to fabricate the samples is derived from a previously published method to fabricate crystalline $MAPbBr_3$ perovskite thin films.[13a] It is a two-step method, in which nucleation and crystallization are separated. First, a film of intermediate material is formed.[13a,c] During the spin coating process, a layered structure is formed, consisting of layers of $PbBr_2$, DMSO, and MABr. In this structure, the $PbBr_2$ functions as a Lewis acid

and DMSO and MABr as Lewis bases.[13d] The resulting intermediate phase is crystalline to an extent, with XRD peaks indicating a unit cell size on the order of a nanometer.[22] The formation of the intermediate phase inhibits the reaction between $PbBr_2$ and MABr, inhibiting crystallization in solution or during spin coating, and thus decreasing the rate of crystallization ($R_{crystallization}$).

When this recipe is used to form polycrystalline perovskite, the crystallization occurs by intercalation of the intermediate phase on the substrate, due to removal of the excess organics within the intermediate phase by annealing.[22a] The perovskite grain size is determined by the amount of nucleation sites within the intermediate film, which depend on spin coating speed and duration.[22b] The quality of the final product is controlled, to a large extent, by the rate of desolvation of the intermediate phase, which in turn determines the rate of growth (R_{growth}). In general, slower desolvation will lead to more homogeneous films. The rate of desolvation can be adjusted by, for example, altering the boiling point of the solvent that's involved in the intermediate phase complexes.[23]

Because many aspects of the final film are determined by the intermediate phase, it is important to investigate the intermediate phase of the amorphous films and its development into the final film. This provides insight into the formation mechanism of amorphous perovskite. XRD measurements of the intermediate phase and of the material after several different short annealing times can be found in **Figure 5**a. The intermediate phase exhibits an XRD peak at $2\theta \approx 8°$. This peak, corresponding with a crystalline compound with a unit cell size larger than a nanometer, is characteristic of a perovskite intermediate phase in which the excess organics and precursors coordinate.[22]

The Fourier transform infrared spectra of intermediate phases of amorphous and crystalline perovskite are largely similar (Section S14, Supporting Information). This is to be expected, because the components are identical, aside from the additional MAAc. Like MABr and DMSO, MAAc has also been shown to form H-bridges with the perovskite precursors, and thus partakes in the intermediate phase. However, small differences can be observed. The most pronounced difference between the spectra is the absorbance peak at $\omega = 1605\ cm^{-1}$, which is very pronounced for the intermediate phase of amorphous perovskite. This peak has previously been observed for perovskite precursor complexes containing MAAc, and therefore proves the larger presence of MAAc within the intermediate phase of amorphous perovskite than of crystalline perovskite.[24]

The differences between the final products can be understood from the rate of desolvation of each intermediate phase. MAAc is more volatile than the other Lewis bases that are components of the organic framework in the intermediate phase.[24] The larger the ratio of MAAc to other components, the more rapidly the desolvation of the intermediate phase occurs. A large fraction of MAAc increases R_{growth}, while $R_{crystallization}$ remains unaltered. When R_{growth} is very large, the process happens too quickly to allow for crystallization, and the ions are trapped into an amorphous structure. The larger the ratio of MAAc to MABr and DMSO in the intermediate phase, the faster the desolvation, and the faster the rate of growth. When enough MAAc is present in the intermediate phase, rapid desolvation occurs and amorphous perovskite is formed. Because the spread of organics is not perfectly homogeneous, one film can have areas in which the ratio is large enough to satisfy the condition, $R_{growth} > R_{crystallization}$, while in other areas the rate of crystallization is the larger. This causes films to combine amorphous and crystalline areas in some cases. Obtaining perfect positional control over these rates, would mean perfect control over the amount and location of incorporated crystalline material within amorphous films. This could be done, for example, by local laser crystallization.

Looking back to Figure 2b, the threshold of incorporation of acetate into the final film can be explained by the increase of the rate of growth. At a certain ratio of MAAc to other organics in the intermediate phase, the desolvation happens so rapidly, increasing R_{growth} beyond the rate at which MAAc can leave the sample. The excess MAAc will then be trapped in a solid film. In this way, it can be both situated in the amorphous material, or the acetate can take the place of the halide within crystalline perovskite (Section S6, Supporting Information). The amount of MAAc at which the R_{growth} surpasses the escape rate of MAAc, determines the threshold for MAAc to be incorporated into the final film.

3. Conclusions

In conclusion, our work sheds light on the properties and formation mechanism of amorphous organic–inorganic halide perovskites. The amorphous thin films form via addition of MAAc to a well-established synthesis method. MAAc causes the formation of amorphous perovskite, by concurrent inhibition of nucleation and crystallization by forming an intermediate phase, and rapid desolvation during annealing. Using this method, it is possible to create amorphous films, as well as films that combine crystalline and amorphous material. Both the crystalline and the amorphous materials formed this way, contain organic A-site cations, lead halide cages, and acetate, which may have partially substituted halides.

The amorphous perovskite phase has a bandgap in the UV, which is tunable by varying the perovskite composition. This approach is broadly applicable to formamidinium, MABr, and iodide amorphous perovskite films, but is not successful with the Cs cation. When crystalline perovskite is incorporated into an amorphous film, the PL properties of the crystalline material are improved, because of a reduction in the concentration of active trap states compared to polycrystalline thin films.

In the future an amorphous perovskite matrix could be used to improve the quality of crystalline halide perovskite in devices such as LEDs or photovoltaics. For these applications, it is vital to obtain precise control over the amount of crystalline incorporations within the amorphous phase. If this is achieved, the amorphous material might prove to be viable as a passivating contact layer, analogous to the amorphous silicon layer in record breaking crystalline silicon solar cells.

4. Experimental Section

Sample Fabrication: MABr (99.999%), $PbAc_2$ (99.999%), FAAc (99%), and DMSO (anhydrous ≥ 99.9%) were purchased from Sigma-Aldrich,

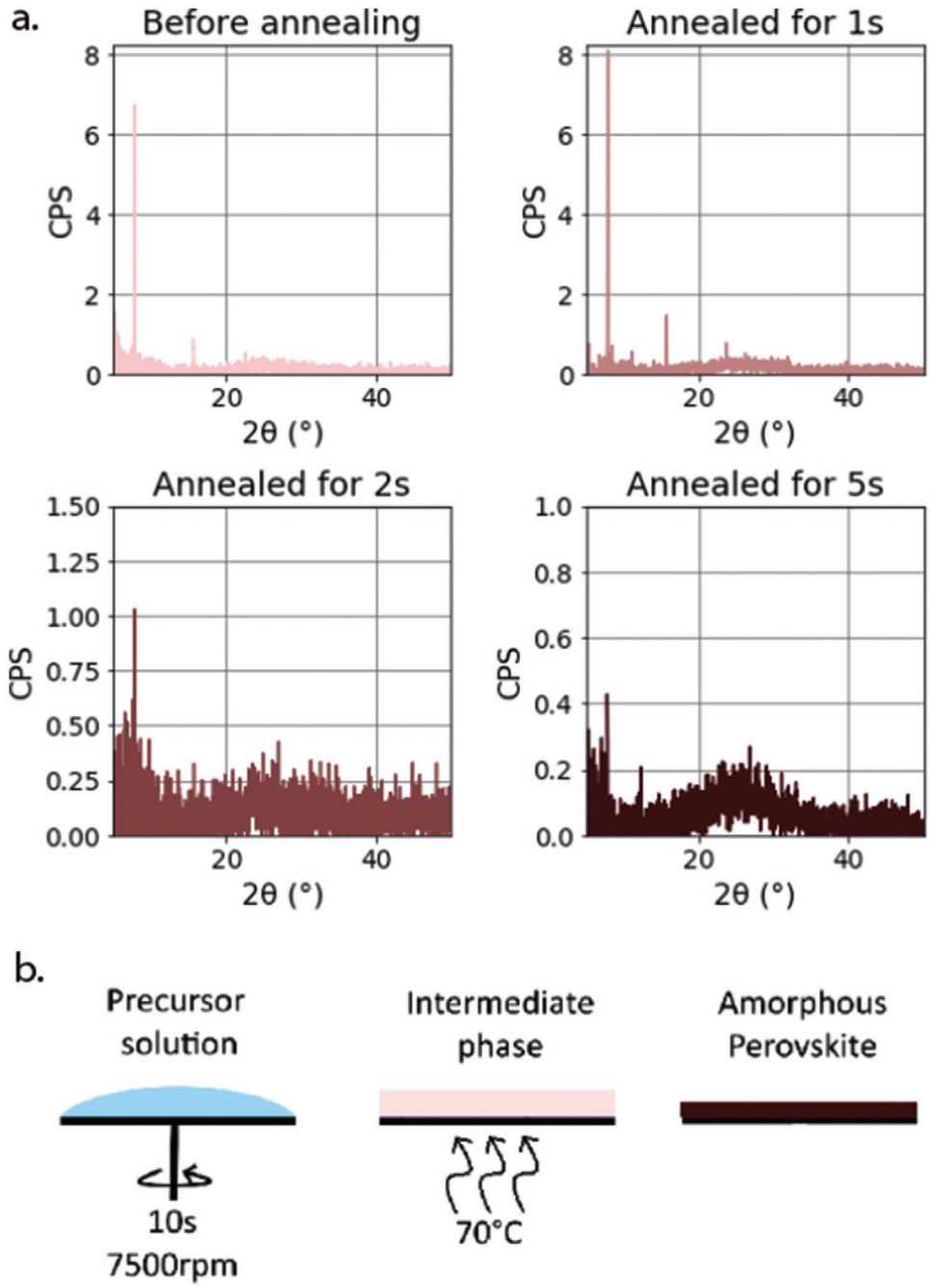

Figure 5. a) XRD pattern of the unannealed intermediate phase, and of the film after several short times of annealing, and b) a cartoon of the formation mechanism of the amorphous perovskite.

MAAc (>98%) was purchased from TCI, formamidinium iodide (FAI) from GreatCell Solar and methylammonium iodide (MAI) from Solaronix. All chemicals were used as received. Samples were prepared on UV/ozone treated silicon and quartz substrates.

Solutions were prepared in a glovebox by dissolving 6 M of organic halide precursor (MABr, MAI, or FAI) and 2 M of $PbAc_2$ in DMSO. To obtain samples labeled 33.3% to 66.7%, a percentage of organic halide precursor was replaced by organic acetate (MAAc or FAAc) precursor, always keeping the combined molarity of organic precursors at 6 M. The precursor solutions were subsequently drop casted, spin coated, and annealed at 70 °C for 2 h.

Characterization: Powder XRD patterns were recorded using a Bruker D2 phaser, equipped with a Cu Kα tube.

Scanning X-ray nano-diffraction microscopy (nano-XRD) experiments were performed with the hard X-ray nanoprobe of the Center for Nanoscale Materials (CNM) at sector 26-ID-C of the Advanced Photon Source, Argonne National Laboratory. The monochromatic and partially coherent incident X-ray beam (photon energy 10.0 keV, λ = 1.240 Å) was focused on the sample, by an Au Fresnel zone plate of 150-µm diameter and 16-nm outermost zone width, with a FWHM spot size of 20–25 nm.[25] Diffraction images were recorded by a Pilatus area detector with 0.5 s exposure at every step that the X-ray beam mapped on the

sample. 0.5–1 µm step size was used for mapping. The thin films were aligned to the 002 Bragg diffraction with respect to the X-ray beam. Microdiffraction image was collected by opening the parallel beam with 50-µm beam size and exposing the beam for 10 s. The 40% MAAc thin film was rocked by ±0.5° to bring the tilted region into diffraction.

Optical microscopy images were taken with a Zeiss axio imager.A2m in dark field mode.

To measure steady-state absorbance spectra, a LAMBDA 750 UV/vis/NIR spectrophotometer (Perkin Elmer) was used, equipped with a deuterium and tungsten excitation source (wavelength range between 250 and 800 nm), an InGaAs detector, and an integrating sphere.

Steady-state PL spectra were measured with a confocal imaging microscope (WITec alpha300 SR). The samples were excited with a 405 nm diode laser (Thorlabs S1FC405). The resulting PL was collected in reflection mode via an objective, filtered with a 488-nm long-pass filter and measured by a spectrometer (UHTC 300 VIS, WITec) connected to a CCD (Andor iDus DV401A BV).

DFT calculations were performed using VASP in order to calculate the optical bandgap of crystalline halide perovskite incorporating acetate.[26] The optical bandgap was calculated at the Γ-point of a $2 \times 2 \times 2$ unit cell by using the HSE06 exchange correlation functional with spin-orbit coupling and an energy cutoff of 500 eV on the PBEsol optimized structures.[27]

SEM images were obtained with a FEI Verios 460 SEM. EDS measurements were performed in a FEI Verios 460 SEM, equipped with an Oxford Instruments EDX detector, at 10 kV and 100 pA.

Time-of-flight secondary ion mass spectroscopy elemental analysis was done on a nanoTOF II (Physical Electronics, US) instrument with a LMIG gun (Bi source) with an ion dose above the static limit (1.17×10^{14} ions cm^{-2}), on sample areas of 40×40 µm. Depicted error bar ratios resulted in three different measurements on three different sample area and on three different days.

PL decay curves were measured with a home-built setup, equipped with a PicoQuant PDL 828 "Sepia II", a PicoQuant HydraHarp 400 multichannel picosecond event timer, and TCSPC module. The used excitation source was a 485 nm pulsed laser (PicoQuant LDH-P-C-485), and the photoemission was filtered with a 500-nm long-pass filter before being detected by a single-photon avalanche diode detector (Micro Photon Devices, MPD-5CTD). The measurements were done under wide-field illumination, using a lens to spread the laser light over an area of about a quarter squared millimeter. Using neutral density filters, the total intensity of the laser light was lowered to 8.5 µW at continuous wave.

PLQY maps were obtained using a home-built integrating sphere setup equipped with a supercontinuum laser (FianiumWL-SC-390-3), combined with an acousto–optic tunable filter and a piezoelectric stage. The signal was measured using both a Thorlabs PDA100A-EC Si detector and a Newport model 818-UV-L photodetector. To distinguish between PL and excitation light, measurements were done twice, using a long-pass filter (Thorlabs FELH500) and a short-pass filter (Thorlabs FESH500). The samples were excited at $\lambda = 480$ nm. Finally, the PLQY was calculated by dividing the map of emitted photons by the map of absorbed photons.

Supporting Information

Supporting Information is available from the Wiley Online Library or from the author.

Acknowledgements

This work is part of the research program AMOLF, which is partly funded by the Dutch Research Council (NWO). Via our membership of the UK's HEC Materials Chemistry Consortium, which is funded by EPSRC (EP/L000202), this work used the ARCHER UK National Supercomputing Service (http://www.archer.ac.uk). This material is based upon work supported by the National Science Foundation under Grant No. DMR-1848371. Use of the Center for Nanoscale Materials and the Advanced Photon Source, both Office of Science user facilities, was supported by the U.S. Department of Energy, Office of Science, Office of Basic Energy Sciences, under contract no. DE-AC02-06CH11357. PM, SRE and RMAH acknowledge financial support by the LINK program of the Dutch province of Limburg and Interreg V-A EMR and the Netherlands Ministry of Economic Affairs within the "Interreg Euro-Maas-Rijn" project (project number EMR23).

Conflict of Interest

The authors declare no conflict of interest.

Data Availability Statement

Research data are not shared.

Keywords

amorphous films, chemical analysis, crystallization, halide perovskite, nucleation, photoluminescence

Received: December 1, 2020
Revised: January 20, 2021
Published online:

[1] T. Matsui, T. Yamamoto, T. Nishihara, R. Morisawa, T. Yokoyama, T. Sekiguchi, T. Negami, *Adv. Mater.* **2019**, *31*, 1806823.
[2] a) G. W. Adhyaksa, L. W. Veldhuizen, Y. Kuang, S. Brittman, R. E. Schropp, E. C. Garnett, *Chem. Mater.* **2016**, *28*, 5259; b) D. W. de Quilettes, S. M. Vorpahl, S. D. Stranks, H. Nagaoka, G. E. Eperon, M. E. Ziffer, H. J. Snaith, D. S. Ginger, *Science* **2015**, *348*, 683; c) M. Grätzel, *Nat. Mater.* **2014**, *13*, 838; d) S. D. Stranks, G. E. Eperon, G. Grancini, C. Menelaou, M. J. Alcocer, T. Leijtens, L. M. Herz, A. Petrozza, H. J. Snaith, *Science* **2013**, *342*, 341; e) S. D. Stranks, H. J. Snaith, *Nat. Nanotechnol.* **2015**, *10*, 391; f) J. S. Yun, A. Ho-Baillie, S. Huang, S. H. Woo, Y. Heo, J. Seidel, F. Huang, Y.-B. Cheng, M. A. Green, *J. Phys. Chem. Lett.* **2015**, *6*, 875.
[3] a) I. Ivanov, A. Steparuk, M. Bolyachkina, D. Tsvetkov, A. Safronov, A. Y. Zuev, *J. Chem. Thermodyn.* **2018**, *116*, 253; b) A. Sharenko, M. F. Toney, *J. Am. Chem. Soc.* **2016**, *138*, 463.
[4] J. Xing, F. Yan, Y. Zhao, S. Chen, H. Yu, Q. Zhang, R. Zeng, H. V. Demir, X. Sun, A. Huan, Q. Xiong, *ACS Nano* **2016**, *10*, 6623.
[5] L. M. Herz, *Annu. Rev. Phys. Chem.* **2016**, *67*, 65.
[6] S. X. Wang, C. H. Bi, J. F. Yuan, L. X. Zhang, J. J. Tian, *ACS Energy Lett.* **2018**, *3*, 245.
[7] a) B. A. Rosales, M. P. Hanrahan, B. W. Boote, A. J. Rossini, E. A. Smith, J. Vela, *ACS Energy Lett.* **2017**, *2*, 906; b) B. A. Rosales, L. Men, S. D. Cady, M. P. Hanrahan, A. J. Rossini, J. Vela, *Chem. Mater.* **2016**, *28*, 6848.
[8] Y. Wang, X. Lü, W. Yang, T. Wen, L. Yang, X. Ren, L. Wang, Z. Lin, Y. Zhao, *J. Am. Chem. Soc.* **2015**, *137*, 11144.
[9] G. W. P. Adhyaksa, S. Brittman, H. Abolins, A. Lof, X. Li, J. D. Keelor, Y. Luo, T. Duevski, R. M. A. Heeren, S. R. Ellis, D. P. Fenning, E. C. Garnett, *Adv. Mater.* **2018**, *30*, 1804792.

[10] K. Yoshikawa, H. Kawasaki, W. Yoshida, T. Irie, K. Konishi, K. Nakano, T. Uto, D. Adachi, M. Kanematsu, H. Uzu, *Nat. Energy* **2017**, *2*, 17032.
[11] E. Amstad, M. Gopinadhan, C. Holtze, C. O. Osuji, M. P. Brenner, F. Spaepen, D. A. Weitz, *Science* **2015**, *349*, 956.
[12] E. C. Sklute, A. D. Rogers, J. C. Gregerson, H. B. Jensen, R. J. Reeder, M. D. Dyar, *Icarus* **2018**, *302*, 285.
[13] a) N. Giesbrecht, J. Schlipf, L. Oesinghaus, A. Binek, T. Bein, P. Müller-Buschbaum, P. Docampo, *ACS Energy Lett.* **2016**, *1*, 150; b) S. Liu, Y. Guan, Y. Sheng, Y. Hu, Y. Rong, A. Mei, H. Han, *Adv. Energy Mater.* **2020**, *10*, 1902492; c) D. T. Moore, H. Sai, K. W. Tan, D.-M. Smilgies, W. Zhang, H. J. Snaith, U. Wiesner, L. A. Estroff, *J. Am. Chem. Soc.* **2015**, *137*, 2350; d) Y. Xia, C. Ran, Y. Chen, Q. Li, N. Jiang, C. Li, Y. Pan, T. Li, J. Wang, W. Huang, *J. Mater. Chem. A* **2017**, *5*, 3193; e) S. Yang, H. Zhao, Y. Han, C. Duan, Z. Liu, S. Liu, *Small* **2019**, *15*, 1904387; f) S. Yuan, Y. Cai, S. Yang, H. Zhao, F. Qian, Y. Han, J. Sun, Z. Liu, S. Liu, *Sol. RRL* **2019**, *3*, 1900220; g) H. Zhao, Y. Han, Z. Xu, C. Duan, S. Yang, S. Yuan, Z. Yang, Z. Liu, S. Liu, *Adv. Energy Mater.* **2019**, *9*, 1902279.
[14] X. Liu, Y. Wang, T. Wu, X. He, X. Meng, J. Barbaud, H. Chen, H. Segawa, X. Yang, L. Han, *Nat. Commun.* **2020**, *11*, 2678.
[15] M. Taguchi, K. Kawamoto, S. Tsuge, T. Baba, H. Sakata, M. Morizane, K. Uchihashi, N. Nakamura, S. Kiyama, O. Oota, *Prog. Photovoltaics* **2000**, *8*, 503.
[16] N. W. Ashcroft, N. D. Mermin, *Solid state physics*, Holt, Rinehart and Winston, New York **1976**.
[17] a) C. Pareja-Rivera, A. L. Solís-Cambero, M. Sánchez-Torres, E. Lima, D. Solis-Ibarra, *ACS Energy Lett.* **2018**, *3*, 2366; b) S. J. Yoon, K. G. Stamplecoskie, P. V. Kamat, *J. Phys. Chem. Lett.* **2016**, *7*, 1368.
[18] K. Tanaka, T. Takahashi, T. Ban, T. Kondo, K. Uchida, N. Miura, *Solid State Commun.* **2003**, *127*, 619.
[19] F. F. Targhi, Y. S. Jalili, F. Kanjouri, *Results Phys.* **2018**, *10*, 616.
[20] W.-J. Yin, J.-H. Yang, J. Kang, Y. Yan, S.-H. Wei, *J. Mater. Chem. A* **2015**, *3*, 8926.
[21] B. R. Sutherland, E. H. Sargent, *Nat. Photonics* **2016**, *10*, 295.
[22] a) W. Zhang, M. Saliba, D. T. Moore, S. K. Pathak, M. T. Hörantner, T. Stergiopoulos, S. D. Stranks, G. E. Eperon, J. A. Alexander-Webber, A. Abate, *Nat. Commun.* **2015**, *6*, 6142; b) G. W. P. Adhyaksa, *Ph.D. Thesis*, University of Amsterdam **2018**; c) N. J. Jeon, J. H. Noh, Y. C. Kim, W. S. Yang, S. Ryu, S. I. Seok, *Nat. Mater.* **2014**, *13*, 897.
[23] B.-E. Cohen, L. Etgar, *Front. Optoelectron.* **2016**, *9*, 44.
[24] L. Chao, Y. Xia, B. Li, G. Xing, Y. Chen, W. Huang, *Chem* **2019**, *5*, 995.
[25] M. Holt, R. Harder, R. Winarski, V. Rose, *Annu. Rev. Mater. Sci.* **2013**, *43*, 183.
[26] G. Kresse, J. Furhmuller, *Phys. Rev. B* **1993**, *47*, 558.
[27] a) J. Heyd, G. E. Scuseria, M. Ernzerhof, *J. Chem. Phys.* **2003**, *118*, 8207; b) A. V. Krukau, O. A. Vydrov, A. F. Izmaylov, G. E. Scuseria, *J. Chem. Phys.* **2006**, *125*, 224106; c) J. P. Perdew, A. Ruzsinszky, G. I. Csonka, O. A. Vydrov, G. E. Scuseria, L. A. Constantin, X. Zhou, K. Burke, *Phys. Rev. Lett.* **2008**, *100*, 136406.